Ionics
https://doi.org/10.1007/s11581-024-05872-z

RESEARCH

Novel platinum-free counter-electrode with PEDOT:PSS-treated graphite/activated carbon for efficient dye-sensitized solar cells

G. K. R. Senadeera[1,2] · **R. M. S. S. Rasnayake**[1,2] · **J. M. K. W. Kumari**[2] · **P. U. Sandunika**[2] · **M. A. K. L. Dissanayaka**[2] · **D. L. N. Jayathilake**[1] · **T. Jaseetharan**[3] · **P. Ekanayake**[4]

Received: 17 June 2024 / Revised: 18 September 2024 / Accepted: 4 October 2024

Abstract

Developing an efficient material as a counter electrode (CE) with excellent catalytic activity, intrinsic stability, and low cost is essential for the commercial application of dye-sensitized solar cells (DSSCs). Photovoltaic properties of DSSCs fabricated with cost-effective, platinum-free CEs composed of various carbon allotrope mixtures—including graphite (GR), activated carbon (AC), and poly(3,4-ethylenedioxythiophene) polystyrene sulfonate (PEDOT:PSS) films—were systematically investigated. DSSCs assembled with PEDOT:PSS/GR/AC showed an impressive photovoltaic conversion efficiency of 4.60%, compared to 4.06% for DSSCs with GR/AC CE or 1.66% for PEDOT:PSS alone or 6.56% for Pt under the illumination 100 mW cm^{-2} (AM 1.5 G) due to the superior electrocatalytic activity and the conductivity of AC and PEDOT:PSS. The fabricated carbon counter electrodes were extensively characterized by using scanning electron microscopy (SEM), X-ray diffraction (XRD), Raman spectroscopy, cyclic voltammetry (CV), Tafel measurements, and electrochemical impedance spectroscopy (EIS). The CV, EIS, and Tafel measurements indicated that the PEDOT:PSS/GR/AC composite film has low charge-transfer resistance on the electrolyte/CE interface and high catalytic activity for the reduction of triiodide to iodide than the GR/AC CEs. It is potentially feasible that such a carbon configuration can be used as a counter electrode, replacing the more expensive Pt in DSSCs.

Keywords Graphite · Activated carbon · PEDOT:PSS counter electrode · Dye-sensitized solar cell

Introduction

Among the third-generation photovoltaic devices, dye-sensitized solar cells (DSSCs) are the most promising photovoltaic devices due to their desired properties such as straight forward fabrication process, environmental friendliness, and adequate efficiency [1–4]. A typical sandwich-structured DSSC consists of three primary components: a dye-adsorbed TiO$_2$ layer on a conductive glass substrate serving as the photoanode, an iodide/triiodide (I$_3$ $^{-}$/I $^{-)}$ redox couple as the electrolyte, and a platinized counter electrode (CE) [5]. The CE plays a crucial role in DSSCs by collecting electrons from the external circuit and catalyzing the reduction of I$_3^-$ to I$^-$. This process demands both excellent catalytic activity and high conductivity from the CE materials [5–7]. Platinum (Pt) and Pt-based materials are currently the standard catalysts for CEs in DSSCs due to their superior electron conductivity and electrocatalytic activity. However, their limited availability, high cost, and instability in iodine-based electrolytes pose significant challenges for large-scale commercial applications of these DSSCs [6, 7]. Therefore, the development CEs of non-noble metal catalysts with competitive electrochemical performance and exceptional stability is essential for advancing sustainable energy technologies and facilitating their broader commercialization [8–10]. In recent years, a variety of alternative materials have been investigated for counter electrodes in DSSCs, aiming to achieve comparable or even superior performance to Pt at a lower cost [9, 10]. Among them, carbonaceous materials [7–14]

✉ G. K. R. Senadeera
gksen@ou.ac.lk

[1] Department of Physics, The Open University of Sri Lanka, Nawala 11222, Nugegoda, Sri Lanka

[2] National Institute of Fundamental Studies, Hantana Road, Kandy 20000, Sri Lanka

[3] Department of Physical Sciences, South Eastern University of Sri Lanka, Sammanthurai 32200, Sri Lanka

[4] Faculty of Science, Universiti Brunei Darussalam, Jalan Tungku Link, Gadong, BE 1410 Brunei Darussalam, Brunei

that have been successfully integrated into DSSCs include graphite [15–17], carbon black [18–24], graphene [25, 26], graphene with metals and alloys [27–31], carbon nanotube [32], carbon dots [33], and transition metal oxides [34, 35]. Apart from that, conducting polymers, including polyaniline (PANI), polypyrrole (PPy), and poly(3,4-ethylenedioxythiophene) (PEDOT), exhibit good electrical conductivity and chemical stability, making them suitable for DSSC applications [36–39]. Among these carbonaceous materials, graphite stands out due to its fascinating properties and frequent use as a catalyst and conducting layer in CEs of DSSCs, and its abundant availability and low cost. Natural graphite is available in three forms amorphous graphite, flake graphite, and crystalline vein graphite each possessing unique properties that suit various applications. Crystalline vein graphite, also known as Sri Lankan graphite, is particularly notable for its naturally occurring rock-like veins and high purity (over 95% pure carbon), high crystallinity, and attractive commercial demand [40]. In 1996, Kay and Gratzel [41] have presented a new type of graphite plus carbon black as a counter electrode with the overall power conversion efficiency of 6.67% under 1 sun. However, large graphite particles with low surface area exhibit very poor catalytic activity when used as counter electrode materials in DSSCs [8]. Graphitic materials, including carbon nanotubes and graphite itself, have two distinct types of planes: basal and edge planes. Basal planes are characterized by slow electron transport, while edge planes enable fast electron transport. Large graphite particles contain fewer edge planes (or more basal planes), which slows down the rate of I_3^- reduction due to high charge transfer resistance (R_{CT}). This high R_{CT} negatively impacts the fill factor (FF) and results in poor energy conversion efficiency (η) in DSSCs [8, 41, 42]. In this context, Veerappan et al. have showed that sub-micrometer size colloidal graphite can be used as an efficient counter electrode catalyst for triiodide reduction in DSSCs and obtained an energy conversion efficiency greater than 6.0%, comparable to the conversion efficiency of Pt [15]. Narudin et al. demonstrated a low-cost carbon black with graphite counter electrode in DSSCs by incorporating binders. They reported a good adherence to the substrates with high conductivity and electrochemical activity was achieved, resulting in an overall efficiency of 5.72% with the CE fabricated using titanium (IV) isopropoxide (TTIP) [19]. Chou and colleagues demonstrated that by increasing the thickness of the graphite/carbon black CE film to 10.4 µm, the efficiency of DSSCs can be enhanced from 0.8 to 1.5% [20]. Don et al. [22] demonstrated that incorporating acetylene carbon black (AB) into graphite catalytically enhances the triiodide ion reduction in DSSCs, significantly improving photo-conversion efficiency from 3.43 to 5.06%. In our recent study, we demonstrated that SnO_2 nanoparticles in graphite/SnO_2 composite counter electrodes enhance the adhesion of vein graphite to conducting glass substrates and increase the effective surface area of the counter electrode by creating a nanoporous structure [35]. Apart from the graphite, polystyrene sulfonate–doped poly-(3,4-ethylenedioxythiophene) (PEDOT:PSS) has also been studied in recent years as an alternative to the Pt based CEs in DSSCs [43, 44,]. This is mainly due to its good electrical conductivity, electro catalytic activity, and good ability to form homogenous CEs. Kitamura and Shiratori demonstrated that layer-by-layer self-assembled mesoporous PEDOT:PSS and carbon black hybrid films can serve as effective platinum-free counter electrodes for DSSCs, achieving 4.7% efficiency, just 8% lower than devices using conventional thermally deposited platinum on fluorine-doped tin oxide glass counter electrodes [42]. Muto et al. [38] reported printable mesoporous counter electrodes using pastes containing PEDOT–PSS solution, TiO_2 nanoparticles, and indium–tin oxide nanoparticles, achieving an efficiency of 4.38%, which is approximately 20% less than the 5.41% efficiency yielded by Pt counter electrodes. Shunjian Xu et al. have developed a nanoporous composite film of TiO_2/SnO_2 and PEDOT:PSS as a counter electrode for DSSCs, achieving a 6.54% efficiency, which is 36.5% higher than that of a cell using a pristine PEDOT:PSS film [26].

By considering above factors, in this study, we focused on developing a composite material that combines PEDOT:PSS, Sri Lankan natural vein graphite (GR), and activated carbon (AC). The primary goal of preparing a mixture counter electrode (PEDOT:PSS/GR/AC) is indeed to find a cost-effective alternative to Pt used in DSSCs. These materials are chosen for their electrocatalytic properties and availability at a lower cost compared to Pt. PEDOT:PSS is relatively inexpensive conducting polymer and widely used in various electronic applications. Sri Lankan vein graphite having high purity, abundancy, the quantities required for DSSC applications are small, and cost-effective production methods are continually being developed. Activated carbon is also a low-cost material with excellent surface area and conductivity, making it an ideal component for a composite electrode in DSSCs. By combining these materials, we aim to improve their individual strengths to create a counter electrode that not only performs well but is also significantly cheaper than Pt. It was observed that, DSSCs fabricated with PEDOT:PSS/GR/AC counter electrodes with TiO_2 binder gives superior photovoltaic properties than the DSSCs fabricated with GR/AC CEs and comparative properties with the traditional expensive Pt CEs in DSSCs. Therefore, by considering the abundance of Sri Lankan graphite, and the incorporation of small amounts of activated carbon and PEDOT:PSS in the CE, coupled with a straightforward fabrication technique, this CE is expected to ultimately render a more cost-effective CE than traditional high-cost Pt based CEs used in DSSCs. Furthermore, incorporating Sri Lankan vein graphite into advanced applications will increase the value of this low-cost raw material, contributing to value addition and promoting economic growth of the country.

Experimental details

Materials

Sri Lankan natural vein graphite collected from "*Bogala*" mines was used as the starting material for graphite (GR). To prepare the photoanodes, Ruthenium N719 dye ($RuL_2(NCS)_2$:2TBA, Solaronix), titanium dioxide P-90 powder (Evonik), titanium dioxide P-25 powder (Degussa), polyethylene glycol (PEG 2000, Merck), triton X-100 (Merck), hydrochloric acid (37%, Merck), and α-terpineol (Sigma-Aldrich) and Titanium(IV) isopropoxide (TTIP) (Sigma-Aldrich) were used as received without further purification. To prepare the electrolyte, iodine chips (I_2), acetonitrile (anhydrous), ethylene carbonate, and propylene carbonate were purchased from Sigma-Aldrich. Fluorine-doped tin oxide (FTO)–conducting glasses (8 Ω/sq, Solaronix) were used as the substrates for both photoanode and counter electrodes.

Photo-anode preparation

A photo-anodes with two layers of TiO_2 on a FTO substrates were prepared by following a procedure reported previously [35]. In brief, for the first compact TiO_2 layer of P90, 0.25 g of P90 TiO_2 powder was ground with 1 ml of 0.1 M HNO_3 in an agate mortar for 20 min. The resulting paste was then spin-coated onto a pre-cleaned FTO glass substrate at 3000 rpm for 60 seconds. The FTO substrate with P90 TiO_2 was then sintered at 450°C for 45 min. After cooling to room temperature, the second layer of mesoporous TiO_2 was prepared by using P25 TiO_2 powder. 0.25 g of TiO_2 powder (P25) was mixed with 1 ml of 0.1 M HNO_3 and ground in a mortar and pestle. Then, 0.02 g of Triton X-100 and 0.05 g of PEG 2000 were added as binders and mixed thoroughly until the mixture formed a creamy paste. This paste was doctor-bladed onto the previously prepared P90 TiO_2 compact layer over a 0.25 cm^2 cell area. Then, the substrate with two types of films was sintered at 450°C for 45 min to obtain a photoanode with porous TiO_2 layer on topside of the FTO. Finally, these photoanodes were dipped independently in ethanolic dye solutions containing 0.3 mM of N719 dye at room temperature for 24 h.

Preparation of counter electrode

The counter electrodes were prepared using Sri Lankan natural vein graphite (GR) flakes sourced from the *Bogala* mines in Sri Lanka. The powdered graphite samples were obtained by following the method outlined by Kumara et al. [40]. Specifically, the graphite flakes were subjected to ball milling for 20 min, followed by sieving to achieve particles smaller than 63 μm. These particles were then dispersed in deionized water with continuous stirring and subsequently agitated for approximately 1 h. The resulting graphite layer that formed on the water surface was collected onto a glass slide and vacuum dried for approximately 12 h. The carbon content of the resulting buoyant graphite powder was analyzed using ASTM-561 methodology and by measuring the residue's weight. The analysis indicated a total carbon content of 99.94%, confirming the high purity of the graphite [40]. The counter electrodes with different amounts of graphite and activated carbon powder were fabricated and tested by varying the amount of activated carbon powder purchased from Aldrich. The best performances in the DSSCs were obtained with the following compositions and further studies were carried out with the same composition. The CEs with best composition were fabricated by using 0.875 g of aforementioned graphite powder and 0.0375 g of active carbon powder and mixed well with 1 ml α-terpineol, 100 μl, TTIP and 10 μl glacial acetic acid (GAA) in an agate mortar for 30 min until homogeneous mixture is formed. Then, creamy paste was doctor bladed on pre-cleaned FTO glass substrate and subjected to annealed at 400 °C for 25 min.

Fabrication of PEDOT:PSS in-cooperated counter electrode

PEDOT:PSS (Baytron, Bayer AG, $\sigma = 8 \times 10^{-2}$ S/cm) was utilized as the starting material. Ethanoic solutions were prepared by mixing absolute ethanol and the PEDOT:PSS solution in a 1:1 volume ratio. Different amounts of this solution was spin coated as follows. At first, this solutions were spin coated at 1500 rpm for 1 min on pre-cleaned FTO glass and FTO/Graphite/AC and then annealed at 80 °C, for 30 min and then at 400 °C for 20 min by following the procedures described by Wen Cai Ng et al. in preparation of PEDOT:PSS/CuO/MoS_2 photocathode [43].

Preparation of liquid electrolyte

The iodide/triiodide-based liquid electrolyte for this study was prepared by dissolving 0.738 g of tetrapropylammonium iodide (Pr_4NI), 0.06 g of iodine (I_2), and 3.6 ml of molten ethylene carbonate (EC) in 1 ml of acetonitrile. The resulting solution was magnetically stirred for 24 h at ambient temperature.

Fabrication of DSSCs and their characterization

DSSCs were fabricated by placing the liquid electrolyte between the TiO_2 photoanodes and the counter electrodes. The active surface area of the device was 0.25 cm^2. The current density–voltage (*J-V*) characteristics of the DSSCs were measured using a computer-controlled, calibrated solar simulator (Oriel Newport LCS-100) connected to a Potentiostat/Galvanostat (Metrohm Autolab PGSTAT 128 N) under AM 1.5 illumination (100 mW cm^{-2}). A Xenon 100 W lamp with an AM 1.5 filter (400–1100 nm). Class A with spectral match of 0.75–1.25 was used to obtain the simulated sunlight with above intensity. In order to compare the performance of DSSCs with graphite-based and Pt-based counter electrodes, DSSCs with the identical TiO_2 photoanode with the same electrolyte were also fabricated using Pt CEs.

Characterization of photoanode and the counter electrode

The surface morphology of the photoanodes and counter electrodes was characterized by scanning electron microscopy (SEM) using Zeiss EVO LS15 scanning electron microscope. The wide-angle X-ray spectroscopy (WAXS) was performed using Rigaku X-ray diffractometer with CuKα radiation (λ = 1.5406 Å). The diffuse reflection spectra were obtained in the wavelength range from 240 to 800 nm using UV-Vis spectrophotometer (Shimadzu 2450) with an integrating sphere attachment. Impedance measurements of DSSCs were taken under 100 mW cm^{-2} illumination using a Potentiostat/Galvanostat (Metrohm Autolab PGSTAT 128 N) with Frequency Response Analyzer (Metrohm Autolab FRA 32) covering the frequency range from 0.01 Hz to 1.0 MHz.

In order to study the electrocatalytic properties of the counter electrode, cyclic voltammetry (CV) experiments were done at a scan rate of 50 mV s $^{-1}$ by using a three-electrode setup having a Pt wire counter electrode, Ag/AgCl reference electrode, and Pt- or FTO/GR/AC–based composite CEs with and without PEDOT:PSS as the working electrode. A solution of acetonitrile prepared with 10 mM LiI, 0.1 M $LiClO_4$, and 1 mM I_2 was used as supporting electrolyte. The Tafel polarization and EIS measurements of counter electrodes were carried out for symmetrical dummy cells composed of the same CE materials (Pt, pristine graphite and PEDOT:PSSs/graphite/AC/composite) on both electrodes with active cell area of 1.0 cm^2. The liquid electrolyte that used to fabricate DSSCs was sandwiched in between the identical counter electrodes for taking Tafel polarization and EIS measurements.

Results and discussion

In order to confirm the existence of the PEDOT;PSS after annealing at 400 °C, FTIR measurements were conducted on PEDOT:PSS films before and after the annealing. Figure 1 shows the FTIR spectra of the spin-coated PEDOT:PSS films with and without sintering processes. The peaks observed at 1624 cm^{-1}, 1523 cm^{-1}, and 1388 cm^{-1} are associated with the vibrational modes of C=C, C–C, and C-O-C bonds. Meanwhile, the peaks at 1197 cm^{-1} and 1085 cm^{-1} correspond to the doped PEDOT, S–O, and S-phenyl groups respectively. The peaks at 972 cm^{-1}, 921 cm^{-1}, 831 cm^{-1}, and 682 cm^{-1} represent the C–S stretching in the sample. [43, 44]. Therefore, as can be seen from Fig. 1, and also as observed by Wen Cai Ng and Men Nang Chong [43], the sintering at 400 °C for short time does not completely decompose the PEDOT:PSS. Although we cannot quantify the remaining undecomposed amount of PEDOT:PSS, our results confirm its presence even after annealing at 400°C for a significantly shorter duration. Therefore, most of the PEDOT:PSS likely remain intact, possibly contributing to the improved performance of the DSSC.

Figure 2 shows the SEM images of (a) the top view and (b) the cross-sectional view of the TiO_2 photoanodes. The photoanode made with P25 nanoparticles has a fairly uniform distribution of TiO_2 nanoparticles of average size around 20 nm as expected. The cross-sectional view of the photoanodes showed a uniform, thicker film with approximately ~ 11.28 µm thickness.

Figure 3(a) shows the surface morphology of the pristine graphite, which lacks the porous structure necessary for effective electrolyte diffusion. This characteristic hinders

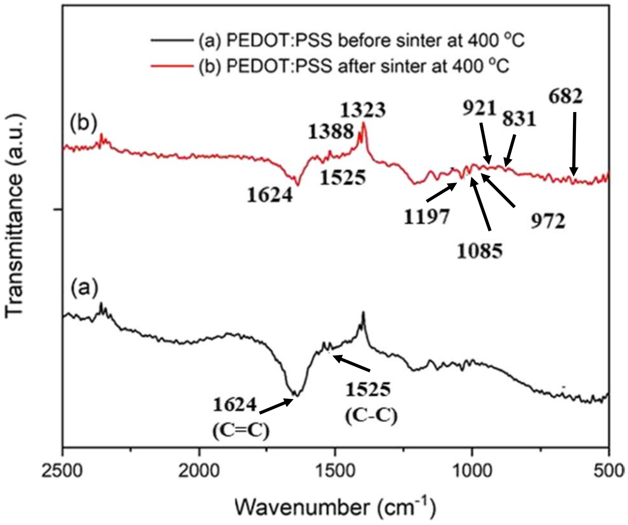

Fig. 1 FTIR spectra of PEDOT:PSS films (**a**) before and (**b**) after annealing

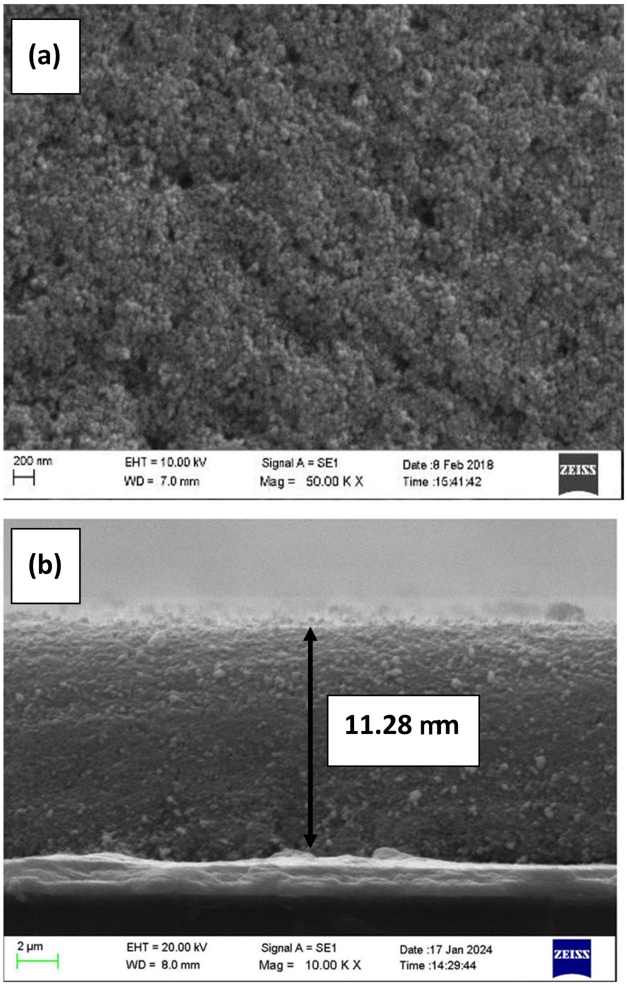

Fig. 2 Scanning electron micrographs of TiO_2 photoanode (**a**) top view and (**b**) cross-sectional view

the efficiency of the iodide/triiodide redox reaction at the counter electrode. The SEM photograph showing surface morphology of the GR/CE counter electrode is shown in Fig. 2(b). The graphite and activated carbon, as well as the TiO_2 crystallite, are fairly uniformly distributed without cracks in the surface. The size of the TiO_2 particles formed by TTIP in GR/AC was found to be relatively smaller at a particle size of approximately ~ 30–40 nm.

Figure 3(c) shows the top view SEM of the composite counter electrode fabricated with PEDOT:PSSs with large number of cracks and voids. As it is observed by Veerappan et al. [15] on the surface morphologies of graphite-based materials in their counter electrodes, it can be concluded that in these PEDOT:PSS–treated CE has more edge planes, i.e., a higher number of catalytic sites than the other GR/AC counter electrode [45]. Figure 4 shows cross-sectional SEM images of (a) GR/AC and (b) PEDOT:PSS/GR/AC. The optimal thickness of the GR/AC counter electrode was determined by testing DSSCs with counter electrodes of

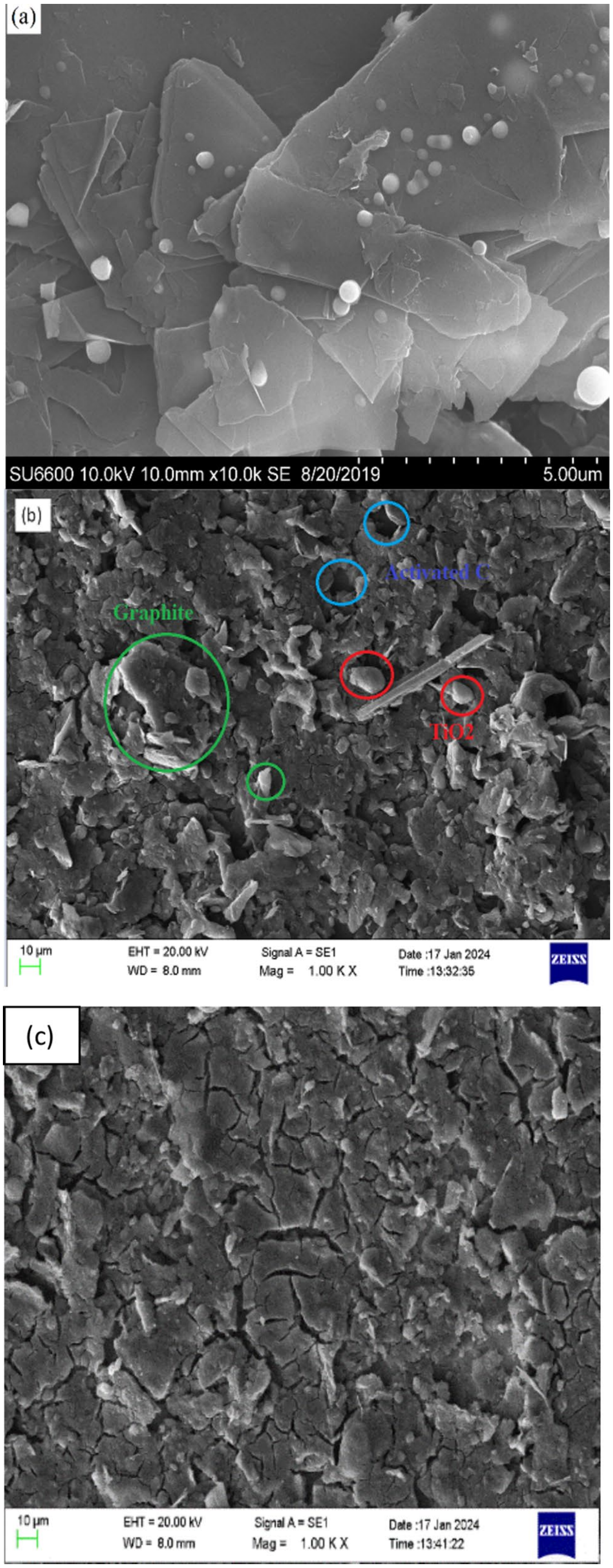

Fig. 3 The top-view SEM images of (**a**) GR, (**b**) GR/AC, and (**c**) / PEDOT:PSS/GR/AC

different thicknesses. As can be seen from Figure 4(a), the optimum thickness was approximately ~ 15.32 µm. Slight increase in the film thickness (~16.00 µm) was observed with the incorporation of PEDOT:PSS layer on the FTO with the optimized composition. The average crystallite size of the GR/AC crystallite is around 500–600 nm. In the production of GR/AC CEs, the GR/AC connectivity and compactness are critical for improving hole extraction and lowering contact resistance in solar cells (Fig. 3(b)). As shown in Fig. 4(a) and (b), large graphite flakes are bound to each other and well packed probably due to the formation of TiO_2 binder and the presence of the activated carbon with large number of pores probably due to the stacking of different materials. Graphite flakes provide good electronic conductivity for the GR/AC CEs, while the activated carbon nanoparticles act as conductive fillers and bridge the gaps among the graphite flakes. Typically, high-porosity carbon films naturally exhibit unique properties, including a large surface area and excellent conductivity. These characteristics are advantageous for electron collection, charge transfer, and ion diffusion [46]. Furthermore, the high porosity can create more active sites, enhancing I^-/I_3^- electro catalytic activity. Therefore, the porous structure shown in Fig. 4(b) with large pores is likely facilitate the diffusion of I_3^- ions to the active sites for reduction. This structure improves the interconnected network on the carbon material surface, resulting in strong adhesion of the electrodes to the FTO substrate, which is beneficial for long-term stability. Similar phenomenon was observed by Don et al. [22] in their counter electrodes fabricated with carbon black/TiO_2 CEs as well as the hydrophilic carbon/TiO_2 colloid composite counter electrodes fabricated by Kouhnavard et al. respectively [47].

Raman spectroscopy is a valuable method for analyzing the structure and quality of carbon materials. It is particularly effective in identifying defects and the ordered or disordered nature of carbon nanomaterials. Figure 5 shows the Raman spectra of the GR/AC and PEDOT:PSS/GR/AC counter electrodes. Two distinct peaks are evident at ~ 1353 cm^{-1} and ~ 1596 cm^{-1}, corresponding to the D and G bands of the carbon materials, respectively [48, 49]. The D band is commonly linked to amorphous carbon and partial disordering of the sp^2 domain, while the G band corresponds to the E_{2g} vibrational mode of the sp^2 hexagonal network plane [47]. Therefore, analyzing the peak intensity ratio of the D to G bands allows for the assessment of the quality of the deposited carbon material. Interestingly, while defective carbon is undesirable for transparent conductive films and device applications, it is advantageous for DSSCs and supercapacitors, as it provides sites that enhance catalytic activity [50].

The calculated Raman peak ratio (I_D/I_G) values are tabulated in Table 1. The larger I_D/I_G ratios obtained for GR/AC with PEDOT:PSS indicates the significant amount of structural defects present in these materials resulting better electrocatalytic activity. As mentioned by Lee et al. defects are advantageous for producing an effective catalytic activity [50]. On the other hand, PEDOT:PSS is a conductive polymer composed of poly(3,4-ethylenedioxythiophene) (PEDOT) and polystyrene sulfonate (PSS). The PEDOT component has a conjugated backbone, which provides excellent electrical conductivity, while PSS serves as a dispersing agent, enhancing the processability and stability of the composite. When PEDOT:PSS is deposited on FTO substrate, it forms a thin film with a high surface area and it may contain numerous nanoscale grains and fibrils due to the self-assembly of PEDOT chains [51]. When applying the mixture of GR and AC by doctor blading technique on to the PEDOT:PSS layer, significant amount of Gr and AC will penetrate in to the nano scale domains of the PEDOT:PSS film due to the solvent nature of the mixture introducing additional structural defects and disorder into the overall composite material. These defects can be due to the interaction between the PEDOT:PSS polymer chains and the GR or AC or both., which disrupts the sp2 hybridized carbon network, leading to an increase in the D band intensity [52]. Therefore, as a result of this, number of edge planes and functional groups might have increased. Edge planes are known to exhibit higher catalytic activity compared to basal planes because of the increased presence of reactive sites [50–52]. Furthermore, intercalation of PEDOT:PSS between graphite layers or adhere to the surface of activated carbon, introducing mechanical strain and causing wrinkling or deformation. This physical alteration of the GR/AC structure contributes to the generation of defects, reflected in the increased I_D/I_G ratio. The presence of PEDOT:PSS can also facilitate the formation of additional sp3 hybridized carbon atoms, further increasing the disorder. Therefore, the increase in the I_D/I_G ratio can be primarily due to the formation of structural defects, enhanced edge planes, intercalation effects, and surface modifications of the GR. These factors collectively result in a material with a higher degree of disorder, which is beneficial for electrocatalytic activity as it provides more active sites for the redox reactions in DSSCs.

Figure 6(a) and (b) shows the XRD spectrum of GR/AC and PEDOT:PSS/GR/AC composites. Here, the presence of narrow and sharp diffraction peak which is centered at ~ 26.6° corresponds to the oriented crystal plane (002) of hexagonal graphite. In addition, less intense peaks at 54.7° (004) suggest the presence of graphite in the material [53, 54]. The XRD pattern shows both anatase and rutile peaks belongs to TiO_2 which has formed due to the incorporation of TTIP as the binder in the fabrication of counter electrode. The low intensity peaks belong to anatase and rutile phases of TiO_2 at 33.67° (101), 37.71° (004), 51.57° (200), 61.58°

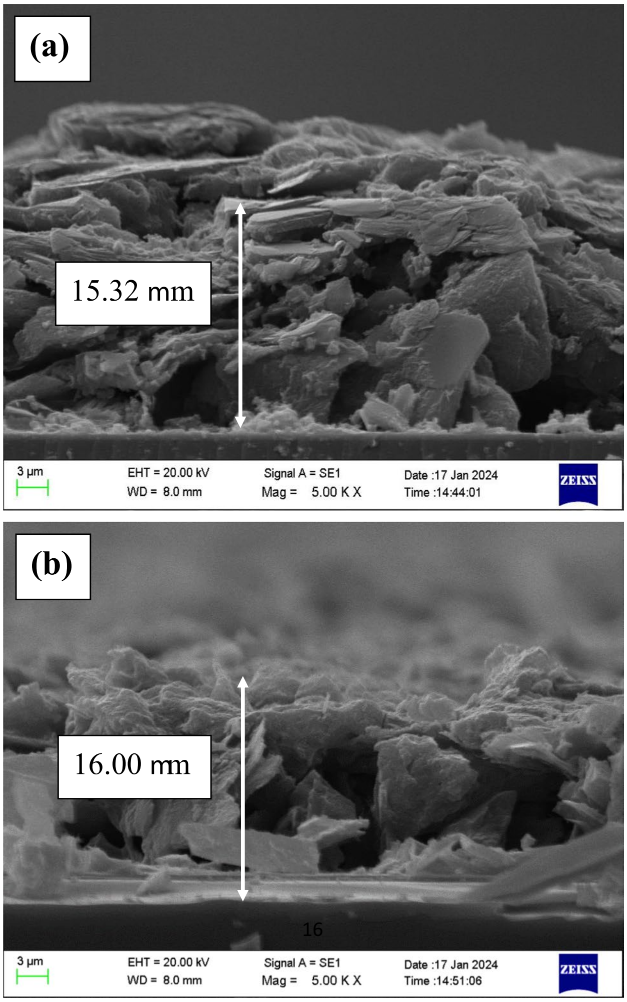

Fig. 4 Cross-sectional SEM images of (**a**) GR/AC and (**b**) PEDOT:PSS/GR/AC

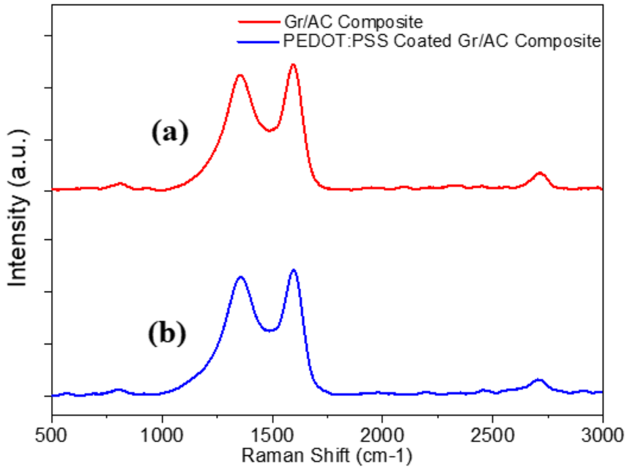

Fig. 5 Raman spectroscopy of (**a**) Gr/AC composite CE, (**b**) PEDOT:PSS–coated Gr/AC composite CE

Table 1 Calculated Raman ratio (I_D/I_G) values for (a) Gr/AC composite CE, (b) PEDOT:PSS–coated Gr/AC composite CE

Counter electrode	D-band (cm^{-1})	G-band (cm^{-1})	I_D/I_G
(a) GR/AC	1355	1596	0.92
(b) PEDOT:PSS/GR/AC	1354	1596	0.95

(204), and 65.50° (002) which can be clearly seen in the figure. Similar peak positions were observed by Xiaoyan Pan in his study on TiO_2/graphite photocatalytic composite [53, 54].

In order to see efficiency variation of the DSSCs with GR/AC counter electrode with different film thickness and the sintering temperature of the composite, DSSCs were fabricated with different thick CEs and also with the different sintering temperatures of them. Since it is not possible to fabricate uniform homogeneous films on the FTO substrate with good adhesive properties, film thickness was varied with two different thickness only. Figure 7 shows the efficiency variation of the DSSCs fabricated with different CE fabricated under different thickness and sintering temperatures. Extracted photovoltaic parameters from the *J-V* characteristic curves for DSSCs with different CS sintered at various temperatures are tabulated in Table 2.

As can be seen from Figure 7 and Table 2, the efficiency increases with increasing sintering temperature up to 400 °C and then decreases. DSSCs fabricated with CEs using two scotch tapes (3m) thickness showed better solar cells efficiencies than the three tapes thickness. As observed from SEM, the best CE film thickness found to be 15.32 µm as depicted in Figure 3(a). This is mainly attributed with the adhesive properties of the material to the FTO as well as the formation of non-uniform CE with higher film thickness than this. It was observed that when DSCS were fabricated with the liquid electrolyte, CEs with thicker films trend to peel off from the FTO substrate. Table 2 shows the photovoltaic parameters extracted from the current voltage characteristics of the DSSC with different CEs sintered at various temperatures. As can be seen from the table, GR/AC counter electrode sintered at 400 °C showed the highest efficiency of 4.06% whereas the DSSCS with Pt CE showed 6.56% efficiency.

The photovoltaic parameters of the DSSCs fabricated with different thickness and sintered at 400 °C are tabulated in Table 3. The data indicates that DSSCs fabricated with CEs of a thickness corresponding to two layers of 3M tape exhibit superior photovoltaic performance compared to those with thicker films. It was observed that as the film thickness increases, adhesion to the substrate decreases, leading to film detachment in the presence of the electrolyte. Conversely, attempts to fabricate CEs with a thickness

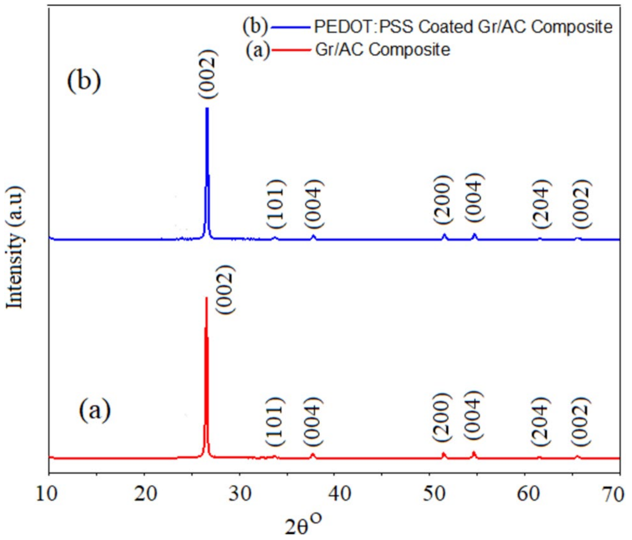

Fig. 6 XRD patterns of two different composites: Graphite/AC and PEDOT:PSS/GR/AC

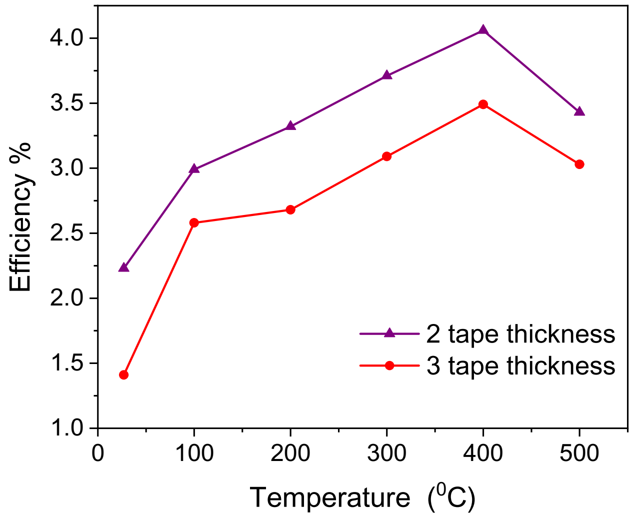

Fig. 7 Efficiency variation of DSCS with two different thick GR/AC counted electrode sintered at different temperatures

less than that of two tape layers resulted in non-uniform films, making it impractical to produce thinner CEs. Consequently, the two-tape thickness was chosen for the CEs. To ensure reproducibility, eight DSSCs were tested for each composition, with the variations in photovoltaic properties documented in the accompanying tables.

Figure 8 shows the current-voltage characteristic of DSSCs fabricated with different CEs including the PEDOT:PSS composite. The photovoltaic parameters are summarized in Table 4. As it is evident from the table due to adhesive problems of the PEDOT:PSS to the FTO substrate in the presence of the electrolyte, DSSCs fabricated with pristine PEDOT:PSS showed poor performances with 1.66% efficiency. However, the DSSCs fabricated with GR/AC incorporated in to PEDOT:PSS CEs showed slightly higher efficiency of 4.60% than the DSSCs with only GR/AC counter electrode.

As illustrated in Table 4, the difference in the *J*sc of DSSCs fabricated with Pt and PEDOT:PSS/GR/AC is minimal. This minor variation could be attributed to the porous structure and surface roughness of the PEDOT:PSS/GR/AC CE as well as the electrocatalytic activity of it. It is well established that the diffusion of iodide ions near the electrode surface can be hindered by a thick layers of CEs [55, 56]. Consequently, increased roughness of the CE enhances the diffusion of triiodide and iodide ions, thereby accelerating the triiodide/iodide redox process. A similar effect was observed by Van-Duong Dao in DSSCs incorporating Pt nanoparticles (PtNPs), Pt-sputtered (PtSP), and Pt hollow counter electrodes [56–58].

Figure 9 shows the comparison of incident photon-to-current conversion efficiency (IPCE) spectra of the DSSCs with (a) Pt and (b) PEDOT:PSS/GR/AC counter electrodes. Table 5 shows a comparison of *J*sc values of the DSSCs fabricated with Pt and PEDOT:PSS/GR/AC estimated from *J-V* and IPCE measurements. The J_{SC} value obtained from J-V characteristics strongly correlated with the estimated J_{SC} value of the DSSC using the IPCE curves. The IPCE of DSSCs measures their spectral response to incident monochromatic light in terms of the generated current. Both DSSCs exhibit strong photoelectric responses within the 300–370 nm range (UV region) and the 375–700 nm range (visible region). The IPCE values in the UV range were primarily due to the absorption of the TiO_2 film, which exhibits an absorption peak around 330 nm corresponding to the direct band gap photoexcitation of electrons [1, 3]. As can be seen from figure, the DSSCs with PEDOT:PSS/GR/AC CE show ~ 54.5% highest IPCE in 400–750 nm range (visible region) which is only ~2.68% lower than that of the DSSC fabricated with Pt CE electrode (54.5%). This suggests that the PEDOT:PSS/GR/AC electrode exhibits strong catalytic properties, making it a promising alternative to Pt as a CE material in DSSCs.

Even though large numbers of research investigations were carried out on the properties of DSSCs with novel carbon-based CEs, very few research investigations have been carried out on the basis of vein graphite. Moreover, in most of the cases, simple fabrication techniques were not in cooperated. Table 6 shows a summary of selected results from the literature on the performance of DSSCs utilizing graphite counter electrodes, alongside the findings from this study. The data in Table 6 indicate that comparable efficiencies in DSSCs can be achieved using the proposed combination of materials study in this study as the counter electrode material.

Table 2 Photovoltaic parameters extracted from the current voltage characteristics of the DSSCs with different CEs sintered at various temperatures

Counter electrode	Sintered temperature (°C)	J_{SC} (mA cm $^{-2}$)	V_{OC} (mV)	FF%	Eff%
GR/AC	Not sintered	5.24 ± 0.02	796.74 ± 0.65	53.51 ± 0.15	2.23 ± 0.05
	100	7.10 ± 0.05	801.93 ± 0.05	52.78 ± 0.25	2.99 ± 0.15
	200	7.79 ± 0.33	796.44 ± 0.45	53.79 ± 0.14	3.32 ± 0.28
	300	8.28 ± 0.06	792.16 ± 0.55	56.66 ± 0.16	3.71 ± 0.14
	400	11.60 ± 0.25	744.31± 0.75	57.59 ± 0.35	4.06 ± 0.03
	500	7.31 ± 0.36	798.27 ± 0.12	58.96± 0.25	3.43 ± 0.15
Pt	Not sintered	13.34 ± 0.15	770.90 ± 0.85	63.99± 0.05	6.56 ± 0.04

Table 3 Photovoltaic parameters of DSSCs fabricated with different thick counter electrodes sintered at 400 °C

Counter electrode	Thickness	J_{SC} (mA cm^{-2})	V_{OC} (mV)	FF%	Eff%
GR/AC	3 tapes	7.64 ± 0.25	804.68 ± 0.16	56.85 ± 0.03	3.49 ± 0.25
GR/AC	2 tapes	11.60 ± 0.25	744.31 ± 0.75	57.59 ± 0.35	4.06 ± 0.05
Pt		13.34 ± 0.15	770.90 ± 0.85	63.99 ± 0.05	6.56 ± 0.04

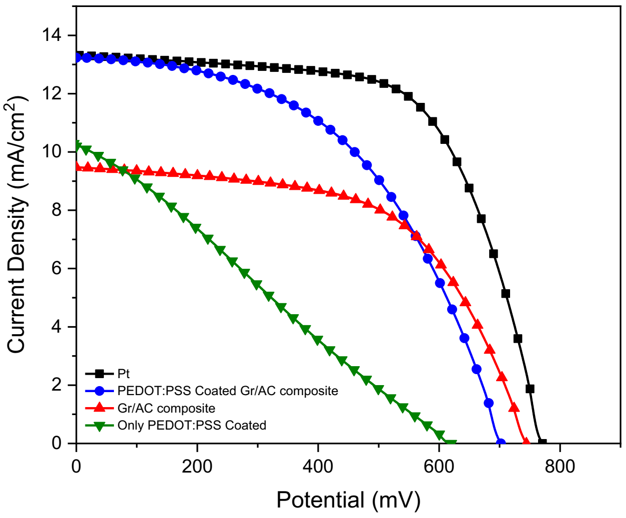

Fig. 8 The current-voltage characteristic of DSSCs fabricated with different CEs including the PEDOT:PSS composite

EIS and equivalent circuit modeling are standard methods for estimating the internal resistance of DSSCs. Within DSSCs, charge carrier transport from the photoanode to the counter electrode encounters several resistive components. These include the series resistance (R_S), which encompasses the sheet resistance of the FTO glass and the contact resistance of the cell; the resistance at the FTO/TiO_2 interface ($R_{FTO-TiO2}$); the electron transport resistance within the TiO_2 film (R_{TiO2}); the charge-transfer resistance associated with electron recombination in the TiO_2 film and I_3^- ions in the electrolyte (R_{CT}); the Warburg impedance representing the Nernstian diffusion of I_3^- ions in the electrolyte (Z_d); the charge-transfer resistance at the counter electrode/electrolyte interface ($R_{CE–electrolyte}$); and the charge-transfer resistance at the exposed FTO/electrolyte interface ($R_{FTO–electrolyte}$). In DSSCs, the charge-transfer resistance at the counter electrode/electrolyte interface ($R_{CE–electrolyte}$) is typically the most significant among these resistive elements. Consequently, R_{CT} often refers specifically to $R_{CE–electrolyte}$ unless otherwise specified. Among these resistances, the series resistance (R_S) and the charge-transfer resistance at the counter electrode/electrolyte interface (R_{CT}) are critically dependent on the counter electrode properties [11, 15, 63, 64]. Specially, the R_{CT} value influences the number of electrons that get transferred from CE to the electrolyte to complete the DSSC circuit. To evaluate the catalytic behavior of the graphitic/AC and PEDOT:PSS incorporated CEs, the charge transfer resistances and sheet resistances of the symmetric cells were measured using EIS. Figure 10 shows the Nyquist plot for both Pt and graphite/AC and PEDOT:PSSs/GR/AC symmetric cells. The R_{CT} and sheet resistance (R_S) were determined through equivalent circuit fitting and calculated values are tabulated in Table 7. As it can be seen from the table, the

Table 4 Solar cell performance of DSSCs fabricated with different counter electrodes

Counter electrode	J_{SC} (mA cm^{-2})	V_{OC} (mV)	FF%	Eff%
Only PEDOT:PSS	10.20 ± 0.01	620.20 ± 0.02	25.82 ± 0.03	1.66 ± 0.02
GR/AC	11.60 ± 0.25	744.31 ± 0.75	57.59 ± 0.35	4.06 ± 0.05
PEDOT:PSS/GR/AC	13.23 ± 0.03	702.20 ± 0.01	59.64 ± 0.02	4.60 ± 0.12
Pt	13.34 ± 0.15	770.90 ± 0.85	63.99 ± 0.05	6.56 ± 0.04

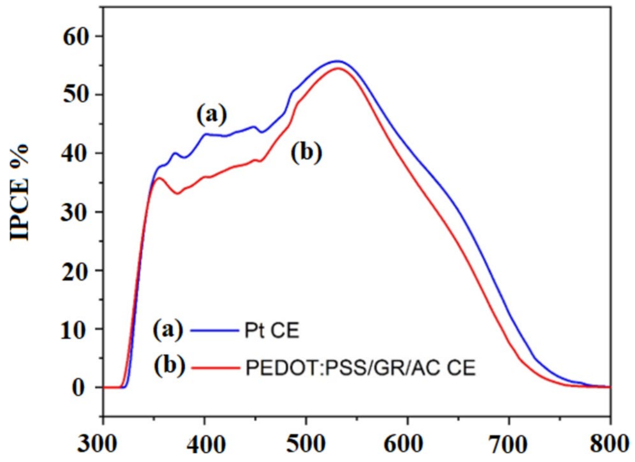

Fig. 9 Comparison of incident photon-to-current conversion efficiency (IPCE) spectra of the DSSCs with (**a**) Pt and (**b**) PEDOT:PSS/GR/AC counter electrodes

Table 5 Comparison of *J*sc values for DSSCs fabricated with Pt and PEDOT:PSS/GR/AC counter electrodes based on *J-V* and IPCE measurements

Counter electrode	J_{SC} (mA cm^{-2}) data from J-V characterization	J_{SC} (mA cm^{-2}) data estimated from IPCE characterization
PEDOT:PSS/GR/AC	13.23 ± 0.03	13.18
Pt	13.34 ± 0.15	13.37

series resistance (R_S) with PEDOT:PSS/GR/AC and GR/AC electrodes are 33.72 Ω and 50.08 Ω respectively. Both values are higher than the R_S value of the Pt electrode (10.9 Ω) This may be due to the lower conductivities of the carbon-based electrodes. On the other hand, as it was observed by Murakami et al. this could be possibly due to the larger thickness and the rougher GR/AC film surfaces [11]. A lower R_S corresponds to a higher conductivity of the counter electrode and a better filling factor of the DSSC which is consistent with our FF values depicted in Table 4 for the Pt CE [64]. Therefore, the DSSC with GR/AC CE showed lower values for the FF, J_{SC}, and lower efficiency than the DSSCs with Pt CE [11, 15]. The charge transfer resistance R_{1CT} or $R_{CE\text{–}electrolyte}$ is an important parameter associated with charge transfer across the electrolyte/CE interface. As expected, the lowest R_{1CT} value of 6.55 Ω shown in Table 7 corresponds to the Pt/electrolyte interface. The GR/AC/electrolyte interface shows much higher R_{1CT} value of 118.4 Ω compared to the Pt/electrolyte interface. This is very likely caused by the higher resistivity of the nanoporous GR/AC composite compared to Pt. The R_{1CT} value of PEDOT:PSS-incorporated CE-based DSSCs is 84.06 Ω and it is much lower than that of the DSSCs with GR/AC counter electrode but much higher than that of the DSSCs with Pt CE. Generally, a decreasing trend in R_{1CT} value is associated with an increasing trend in J_{SC} for most of the DSSC systems studied [54]. The higher efficiency in DSSCs with PEDOT:PSS composite mainly results from higher catalytic activity which is assigned to faster diffusion of redox couple in the electrolyte as observed by the Wu et al. [13]. Incorporation of PEDOT:PSS in GR/AC counter electrode results in higher performance which mainly arises from the higher J_{SC}. The enhanced J_{SC} is mainly results from higher electro catalytic activity owing to lower R_{CT} and diffusion resistance which is in line with the above morphological and electrochemical analysis [62–66].

CV measurements and analysis provide an important and efficient tool for analyzing ion diffusivity and the catalytic mechanism undergoing in an electrochemical system [64–66]. The cyclic voltammetry analysis for electrodes was carried out by a three-electrode system. Figure 11 shows the cyclic voltammograms of Pt, GR /AC, and PEDOT:PSS/GR/AC electrode, in which the potential ranged from −0.2 to 1.2 V (vs. Ag/AgCl) at the scan rate of 50 mV s^{-1}. Two pairs of redox peaks were observed in the cyclic voltammograms of all the CEs. The relative negative pair was assigned to the redox reaction as in Eq. (1) and the positive one was assigned to the redox reaction in Equation (2) [67].

Table 6 Comparison of the performances of graphite-based CEs in literature with the present work

Materials	Method of fabrication	Efficiency (%)	Electrolyte	Reference
GR/AC/PEDOT:PSS	Doctor blade	4.6	I^-/I_3^-	This work
Sub-micrometer sized Graphite	Screen printing	3.2 -6.2	$I\text{-}/I_3^-$	[7]
Activated carbon	Coating/doctor blade	3.89	I^-/I_3^-	[59]
Expanded graphite/pencil-lead	Doctor blading	7.67	I^-/I_3^- (with ionic liquid)	[17]
Flake graphite	Doctor blading	1.57	I^-/I_3^-	[60]
Graphite	Doctor blading	1.33	I^-/I_3^-	[60]
graphite/carbon black	Spray method	1.5	I^-/I_3^-	[61]
Graphite	coating	0.99	I^-/I_3^-	[62]
Vein graphite	spraying	6.47	I^-/I_3^- (with ionic liquid)	[16]
Graphite/carbon black	Doctor blade	3.43 to 5.06%.	I^-/I_3^-	[22]

$$I_3^- + 2e- \rightleftharpoons 3I^- \tag{1}$$

$$3I_2 + 2e- \rightarrow 2I_3^- \tag{2}$$

In DSSCs, the reduction reaction of triiodide (I_3^-) occurs at the counter electrode, which is crucial for completing the circuit and regenerating the dye molecules. Therefore, it is essential to study the redox behavior of the iodide/triiodide (I^-/I_3^-) couple at negative potentials [68]. It has been reported that the electrocatalytic performance of a counter electrode for the reduction of I_3^- in DSSCs is related to the cathodic peak current observed at more negative potentials. A higher cathodic peak current density indicates better catalytic activity of the counter electrode [68–72]. Apart from the as peak current density, counter electrode catalytic ability is estimated using peak-to-peak separation (ΔE_{pp}) of the oxidative and reduction peaks [68]. The peak-to-peak separation is calculated from Equation (3)

$$\Delta Epp = \left| E_p(anodic) - E_p(cathodic) \right| \tag{3}$$

Table 8 shows the estimated electrochemical parameters including the $|\Delta E_{pp}|$ and the diffusion coefficient values of different counter electrodes obtained from CV measurements. The both lower $|\Delta E_{pp}|$ and the V_{OC} of the DSSCs with PEDOT:PSS/GR/AC clearly correlates and indicates the lower electron ejection efficiencies from the PEDOT:PSS/GR/Ac CE than that of the Pt CE. Similar trend in the V_{OC} and $|\Delta E_{pp}|$ was observed by the Van-Duong Dao [72] confirming the positive shift in the I_3^-/I^- redox energy level resulting in the decrease of V_{OC} in DSCs fabricated with hollow sphered and sputtered Pt CEs in DSSCs [71] .

Table 7 Series resistance (R_S) and the charge transfer resistance R_{1CT} ($R_{CE\text{–}electrolyte}$) values of DSSCS with different Ces

Counter electrode	*Rs (Ω)*	R_{1CT} *(Ω)*
GR/AC	50.08 ± 0.25	118.24 ± 0.42
PEDOT:PSS/GR/AC	33.72 ± 0.18	84.06 ± 0.31
Pt	10.60 ± 0.32	9.11 ± 0.23

The reduction current peaks (cathodic peak) of the PEDOT:PSS/GR/AC electrode were much higher than that of the both Pt and the GR/AC electrodes. On the other hand, the reduction peak current density of GR/AC–based electrodes was also much greater than that of the Pt counter electrode. This could be attributed to the large active surface area of both the GR/AC and PEDOT:PSS/GR/AC electrodes. The higher the cathodic peak current density, the better the catalytic activity of the counter electrode [67–73]. Moreover, the $|J_{OX1}|/|J_{RED1}|$ ratio is a parameter which is important in estimating the reversibility of the I^-/I_3^- redox reaction [64]. The value of $|J_{OX1}|/|J_{RED1}|$ for the PEDOT:PSS/GR/AC is much closer to 1.00 than the corresponding values for the GR/AC CE, or even for the Pt cathode, suggesting that the reversible redox reaction $I^- \rightarrow I_3^-$ is more stable on the PEDOT:PSS/GR/AC electrode than on the Pt electrode and the GR/AC electrode [64]. Based on the cyclic voltammetry results, the incorporation of PEDOT:PSS improves the catalytic activity of the composite CE. Similar behavior of these parameters was also observed by Wu et al. in their studies on polyoxometalate-doped polypyrrole film electrodes [63] as well as by Duan et al. with metal selenide alloy CEs in DSSCs [64]. For a real DSSC device, a higher reversibility implies the rapid conversion of I_3^- into I^- species for dye

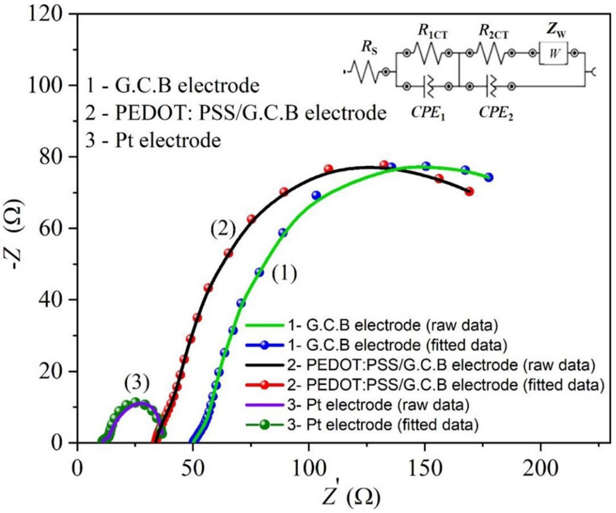

Fig. 10 Nyquist plot for both Pt and graphite/Ac and PEDOT:PSSs/GR/AC symmetric cells

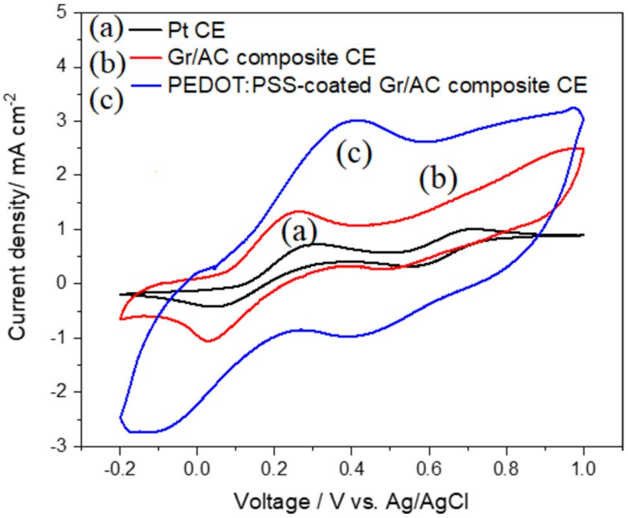

Fig. 11 Cyclic voltammograms of (**a**) Pt, (**b**) Gr/AC, and (**c**) PEDOT:PSS/GR/AC counter electrodes.

recovery. Therefore, more N719 molecules can excite electrons for electricity generation as observed with the highest J_{SC} in DSSCs fabricated with PEDOT:PSS/GR/AC counter electrode. The correlation among peak current density (J_{RED1}), diffusion coefficient (D_n), and scan rate (v) can be expressed by the Randles-Sevcik Equation 4.

$$J_{RED1} = KAC\, n^{1.5}\, D_n^{0.5}\, v^{0.5} \tag{4}$$

where K is a constant ($= 2.69 \times 10^5$), n is the number of electrodes contributing to charge transfer, A is the electrode area, and C represents the bulk concentration of redox species [73–75]. Tafel polarization of all three counter electrodes was performed to further analyze the charge transfer kinetics at the interface of CE/electrolyte using a symmetric cell configuration. The polarization curves display the logarithmic current density as depicted in Fig. 12.

In the equilibrium state, the electron transfer rate can be determined from the intersection of the linear cathodic and anodic branches of the curves, which indicates the exchange current density (J_O) [76]. The J_O is an essential indicator of the catalytic activity of the counter electrode. This is used to assess its effectiveness in reducing iodide ions. A higher J_O value denotes greater catalytic activity of the counter electrode for iodide ion reduction [76]. J_O is inversely proportional to R_{CT} with the following equation. $J_O = RT/nFR_{CT}$, where R is the gas constant, T is the absolute temperature, F is the Faraday's constant, and R_{CT} is the charge transfer resistance [76]. Furthermore, the limiting diffusion current density (J_{lim}), corresponding to the intersection of the cathodic branch with the Y-axis, is a parameter directly proportional to the diffusion coefficient (D_n) of the I^-/I_3^- redox couple at the CE/electrolyte interface. This parameter can be used to estimate the diffusion performance of the redox couples. The highest J_{lim} demonstrates the faster diffusion rate of the I_3^- reduction in the electrolyte. The trends of J_{lim} would consistent with the *J*o for all CEs. The exchange current density (J_O) can be calculated from the polarization region, while J_{lim} can be measured from the diffusion region. The D_n value is directly proportional to diffusion coefficient (D_n) of the I^-/I_3^- redox couple at the CE/Electrolyte interface [76, 77] as shown in Equation 5.

$$D_n = L(J_{lim})/2nFC \tag{5}$$

where *D*n is the diffusion coefficient of I_3^-, L is the thickness of diffusion layer, and C is the concentration of I_3^- [52]. Estimated J_O values and J_{lim} values are tabulated in Table 9.

The J_O value of the cells with GR/AC, PEDOT:PSS/GR/AC, and Pt electrode is approximately 0.85 mA cm^{-2} and 1.04 mA cm^{-2} and 1.84 mA cm^{-2} respectively. This indicates that the PEDOT:PSS/GR/AC CEs in the DSSCs can handle the back reaction more efficiently than the GR/AC counter electrode, and contribute toward improving the current in the device as observed in the J_{SC} values depicted in Table 4. However, the low values of J_O than the Pt CE indicate the lower conductivity in comparison with that of the Pt CEs. Essentially, J_{lim} is a measure of the overall catalytic activity and electron transfer rate, while D_n specifically reflects the ease with which ions diffuse through the material [76, 77]. The Tafel studies as shown in Fig. 12 and Table 8 indicate that J_{lim} for Pt is higher than that for PEDOT:PSS/GR/AC. This higher J_{lim} for Pt is expected due to its superior catalytic properties, which facilitate faster electron transfer reactions, resulting in higher current densities. The CV studies show that the diffusion coefficient, D_n for PEDOT:PSS/GR/AC is higher than that for Pt. This might seem contradictory at first glance, but there may be several factors could contribute to this observation such as different surface area and porosity, microstructure differences, creating additional conductive pathways. etc., that facilitate faster ion movement, thereby increasing the D_n. PEDOT:PSS/GR/AC composites often have higher surface areas and porosities compared to Pt. This increased surface area provides more active sites and pathways for ion diffusion, effectively increasing the D_n. The microstructural differences between the materials can significantly impact the diffusion process. Therefore, while Pt exhibits a higher J_{lim} due to its excellent electrocatalytic activity, the D_n for PEDOT:PSS/GR/AC can still be higher if the composite structure provides more efficient ion transport. Similar results for the J_O and J_{lim} values of the Pt electrodes were observed by several authors like Wei et al. [78] and Yue et al. [79].

Table 8 Electrochemical parameters of different counter electrodes obtained from CV measurements

Counter electrode	$\lvert J_{OX1}\rvert$ (mA cm^{-2})	$\lvert J_{RED1}\rvert$ (mA cm^{-2})	$\lvert J_{OX1}\rvert/\lvert J_{RED1}\rvert$	$\lvert \Delta E_{pp}\rvert$ (V)	D_n ($\times 10^{-4}$)/cm^2 s^{-1}
PEDOT:PSS/GR/AC	2.98	2.85	1.05	0.02	14.21
GR/AC	1.34	1.04	1.29	0.22	1.89
Pt	0.60	0.49	1.22	0.13	0.42

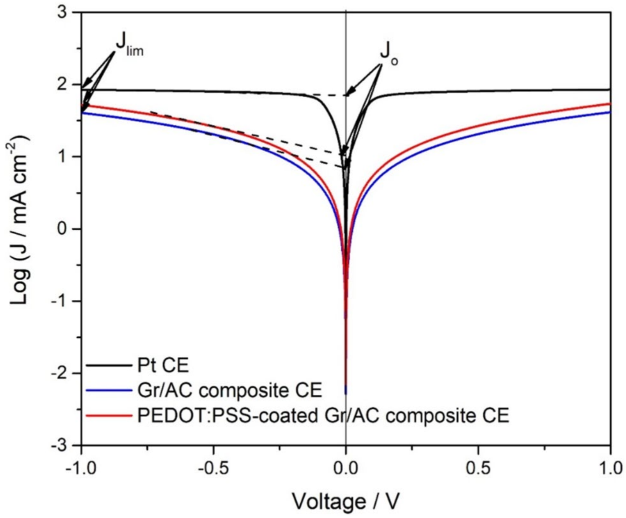

Fig. 12 Tafel curves for all the CEs (**a**) Pt, (**b**) GR/AC, and (**c**) PEDOT:PSS/GR/AC

Table 9 Electrochemical parameters of different electrodes extracted from EIS measurements and Tafel plot measurements

Counter electrode	log J_O (mA cm^{-2})	log J_{lim} (mA cm^{-2})
GR/AC	0.85	1.60
PEDOT:PSS/GR/AC	1.04	1.73
Pt	1.84	1.95

Conclusions

In this study, we developed a novel three-component composite carbon counter electrode (tri-carbon) utilizing Sri Lankan vain graphite, activated carbon, and PEDOT:PSS, which can be used to improve the electrochemical performance of graphite. The combination of PEDOT:PSS with graphite (GR) and activated carbon (AC) in the composite counter electrode further amplifies the number of catalytic sites. Graphite provides additional edge planes and conductive pathways, while activated carbon contributes to the high surface area and porosity. This synergistic effect results in a composite material with a significantly higher number of active sites compared to individual components. The integration of activated carbon and PEDOT into the graphite matrix reduced charge transfer resistance, leading to an increase in J_{SC} and consequently improved electrocatalytic activity and charge transport, as evidenced by EIS and Tafel measurements. DSSCs assembled with the tri-carbon counter electrode (PEDOT:PSS/GR/AC), GR/AC, and Pt counter electrode with Ru N719 dye-sensitized photoanodes achieved efficiencies of 4.60%, 4.0%, and 6.05% respectively. Our results indicate that the composite materials incorporating PEDOT:PSS have significant potential for DSSC applications and warrant further investigation.

Acknowledgements The authors gratefully acknowledge the Open University of Sri Lanka, National Institute of Fundamental Studies, Sri Lanka, and research grant UBD/RSCH/1.4/FICBF(b)/2022/040 for providing necessary financial assistance and the infrastructure facilities.

Author contribution G.K.R. Senadeera and P. Ekanayake were responsible for funding acquisition, resources, conceptualization, and writing the original draft. Formal analysis, investigation, data curation, and visualization were carried out by R.M.S.S. Rasnayake, J.M.K.W. Kumari, P.U. Sandunika, D.L.N. Jayathilake, and T. Jaseetharan. Methodology, validation, project administration, and supervision were managed by G.K.R. Senadeera, M.A.K.L. Dissanayaka, and P. Ekanayake. All authors contributed to validation, reviewed the manuscript, and agreed to its publication.

Data Availability No datasets were generated or analysed during the current study.

Declarations

Competing interests The authors declare no competing interests.

References

1. Grätzel M (2003) Dye-sensitized solar cells. J PhotochemPhotobiol C: Photochem Rev 4:145–153. https://doi.org/10.1201/b19148
2. Arkan F, Pakravesh F, Darband B, Sabagh S, Izadyar M (2024) Recent progress toward high-performance dye-sensitized solar cells: a review. J Iran Chem Soc 21:577–638. https://doi.org/10.1007/s13738-024-02967-2
3. Sharifi N, Tajabadi F, Taghavinia N (2014) Recent developments in dye-sensitized solar cells. ChemPhysChem 15:3902–3927. https://doi.org/10.1002/cphc.201402299
4. Jagtap CV, Kadam VS, Mahadik MA, Jang JS, Chaure NB, Pathan HM (2022) Effect of binder concentration and dye loading time on titania based photoanode in dye sensitized solar cell application. Eng Sci 17:133–141. https://doi.org/10.30919/es8d581
5. Wu J, Lan Z, Lin J, Huang M, Huang Y, Fan L, Luo G, LinY XY, Wei Y (2017) Counter electrodes in dye-sensitized solar cells. Chem Soc Rev 46:5975–6023. https://doi.org/10.1039/c6cs00752j
6. Theerthagiri J, Senthil AR, Madhavan J, Maiyalagan T (2015) Recent progress in non-platinum counter electrode materials for dye-sensitized solar cells. ChemElectroChem 2:928–945. https://doi.org/10.1002/celc.201402406
7. Karim F, Sikder A, Ghann W, Green K, Ozturk B, Ali MM (2020) Uddin J, Nanostructured dye sensitized solar cells with different counter electrodes American. J Phys Chem 9(1):1–8. https://doi.org/10.11648/j.ajpc.20200901.11
8. Imoto K, Takahashi K, Yamaguchi T, Komura T, Nakamura J, Murata K (2003) High-performance carbon counter electrode for dye-sensitized solar cells. Solar Energy Mater Solar Cells 79(4):459–469. https://doi.org/10.1016/S0927-0248(03)00021-7
9. Bu IYY, Hu TH (2016) The role of various carbon nanomaterials for dye-sensitized solar cells applications. Sol Energy 130:81–88. https://doi.org/10.1016/j.progsolidstchem.2017.02.001
10. Denaro T, Baglio V, Girolamo M, Antonucci V, Arico MF, Ornelas R (2009) Investigation of low cost carbonaceous materials

for application as counter electrode in dye-sensitized solar cells. J Appl Electrochem 39:2173–2179. https://doi.org/10.1007/s10800-009-9841-2

11. Murakami TN, Gratzel M (2008) Counter electrodes for DSC: application of functional materials as catalysts. Inorganica Chim Acta 361:572–580. https://doi.org/10.1016/j.ica.2007.09.025
12. Kouhnavard M, Ludin NA, Ghaffari BV, Sopian K, Ikeda S (2015) Carbonaceous materials and their advances as a counter electrode in dye-sensitized solar cells: challenges and prospects. Chemsuschem 8:1510–1533. https://doi.org/10.1002/cssc.201500004
13. Wu M, Lin X, Wang T, Qiu J, Ma T (2011) Low-cost dye-sensitized solar cell based on nine kinds of carbon counter electrodes. Energy Environ Sci 4:2308–2315. https://doi.org/10.1039/C1EE01059J
14. Imotoa K, Takahashi K, Yamaguchi T, Komura T, Nakamura JI, Muratad K (2023) High-performance carbon counter electrode for dye-sensitized solar cells. Solar Energy Mater Solar Cells 79:459–469. https://doi.org/10.1016/S0927-0248(03)00021-7
15. Veerappan G, Bojan K, Rhee SW (2011) Sub-micrometer-sized graphite as a conducting and catalytic counter electrode for dye-sensitized solar cells. ACS Appl Mater Interfaces 3:857–862. https://doi.org/10.1021/am101204f
16. Jayaweera EN, Kumara GRA, Pitawala HMGTA, Rajapakse RMG, Gunawardhana N, Bandara HMN, Senarathne A, Ranasinghe CSK (2017) Vein graphite-based counter electrodes for dye-sensitized solar cells. J Photochem Photobiol A: Chem 344:78–83. https://doi.org/10.1016/j.jphotochem.2017.05.009
17. Wei YS, Jin QQ, Ren TZ (2011) Expanded graphite/pencil-lead as counter electrode for dye-sensitized solar cells. Solid-State Electron 63:76–82. https://doi.org/10.1016/j.sse.2011.05.019
18. Chou HT, Lien CH, Wu DH, Hsu HC and Huang MH (2013) The different film thicknesses of graphite/carbon black on the counter electrodes by spray coating method for dye-sensitized solar cells, 13th IEEE International Conference on Nanotechnology (IEEE-NANO 2013, Beijing, China,pp. 1151-1154, https://doi.org/10.1109/NANO.2013.6720989.
19. Narudin N, Ekanayake P, Soon YW, Nakajima H, Lim CM (2021) Enhanced properties of low-cost carbon black-graphite counter electrode in DSSC by incorporating binders. Sol Energy 225:237–244. https://doi.org/10.1016/j.solener.2021.06.070
20. Chou HT, Lien CH, Wu DH , Hsu HC, and Huang MH (2013) The different film thicknesses of graphite/carbon black on the counter electrodes by spray coating method for dye-sensitized solar cells, 13th IEEE International Conference on Nanotechnology (IEEE-NANO 2013), Beijing, China, pp. 1151-1154, https://doi.org/10.1109/NANO.2013.6720989
21. Murakami TN, Ito S, Wang Q, Nazeeruddin MK, Bessho T, Cesar I (2006) Highly efficient dye-sensitized solar cells based on carbon black counter electrodes. J Electrochem Soc 153:A2255–A2261. https://doi.org/10.1149/1.2358087
22. Don MF, Ekanayake P, Nakajima H, Mahadi AH, Lim CM, Atod A (2019) Acetylene carbon black-graphite composite as low-cost and efficient counter electrode for dye-sensitized solar cells (DSSCs). Ionics 25(11):5585–5593. https://doi.org/10.1007/s11581-019-03071-9
23. Note: This is mandatory.
24. Kim JM, Rhee SW (2012) Electrochemical properties of porous carbon black layer as an electron injector into iodide redox couple. Electrochim Acta 83:264–270. https://doi.org/10.1016/j.electacta.2012.07.107
25. Wang H, Hu YH (2012) Graphene as a counter electrode material for dye-sensitized solar cells. Energy Environ Sci 5:8182–8188. https://doi.org/10.1039/C2EE21905K
26. Xu S, Luo Y, Zhong W, Liu X, Xiao Z, Luo Y (2013) Improved performances of graphite counter electrode for dye-sensitized solar cells by incorporating graphene nanosheets. Appl Mech Mater 253–255:689–692. https://doi.org/10.4028/www.scientific.net/AMM.253-255.689
27. Dao VD, Jung SH, Kim JS, Tran QC, Chong SA, Larina LL, Choi HS (2015) AuNP/graphene nanohybrid prepared by dry plasma reduction as a low-cost counter electrode material for dye-sensitized solar cells. Electrochim Acta 156(20):138–146
28. Dao VD, Larina LL, Lee JL, Jung KD, Huy BT, Choi HS (2015) Graphene-based RuO2 nanohybrid as a highly efficient catalyst for triiodide reduction in dye-sensitized solar cells. Carbon 81:710–719. https://doi.org/10.1016/j.carbon.2014.10.012(ok)
29. Dao VD, Larina LL, Lee JL, Suh H, Hong K, Lee JK, Choi HS (2014) Optimum strategy for designing a graphene-based counter electrode for dye-sensitized solar cells. Carbon 77:980–992. https://doi.org/10.1016/j.carbon.2014.06.015
30. Park E, Lee Y, Dao VD, Cam NTD, Choi HS (2017) Design of CoNi alloy/graphene as an efficient Pt-free counter electrode in liquid junction photovoltaic devices. Synth Metals 230:97–104. https://doi.org/10.1016/j.synthmet.2017.06.002
31. Oha HJ, Dao VD, Ryu KH, Lee JH, Choi HS (2018) FeSn alloy/graphene as an electrocatalyst for the counter electrode of highly efficient liquid-junction photovoltaic devices. J Alloys Comp 754:139–146. https://doi.org/10.1016/j.jallcom.2018.04.227
32. Dang HLT, Tran NA, Dao VD, Vu NH, Quang DV, Ha H, Vua Nguyen TH, Pham TD, Hoang HC, Nguyen HT, Tuan PA (2020) Carbon nanotubes-ruthenium as an outstanding catalyst for triiodide ions reduction. Synth Metals 260:116299. https://doi.org/10.1016/j.synthmet.2020.116299
33. Anh TN, Thi D, Hai Linh H, Linh NH, Hien NT, Hanh NT, Vu NH, Ha VTH, Giang TTH, Tan TVT (August 2024) Dao VD (2024) Robust carbon dots-wrapped NiCo flower-like nanostructures for enhanced triiodide reduction. J Electroanal Chem 967(15):118441. https://doi.org/10.1016/j.jelechem.2024.118441
34. Dao VD, Quang DV, Vu NH, Vu HHT, Ho ND, Duo VT, Hieu NV, Nguyen TH (2019) Tran NA (2019) Transition metal oxides as Pt-free counter electrodes for liquid-junction photovoltaic devices Vietnam. J Chem 57(6):784–791. https://doi.org/10.1002/vjch.2019000114
35. Dissanayake MAKL, Kumari JMKW, Senadeera GKR, Anwar H (2021) Low cost, platinum free counter electrode with reduced graphene oxide and polyaniline embedded SnO_2 for efficient dye sensitized solar cells. Sol Energy 230(2021):151–165. https://doi.org/10.1016/j.solener.2021.10.022
36. Magu TO, Augustine AU, Hitletr L, Dass PM (2019) A review on conducting polymers-based composites for energy storage application. J Chem Rev 1(1):19–34. https://doi.org/10.33945/SAMI/JCR.2019.1.1934
37. Nawarathna HMCP, Abeysingha DUSN, Wickramasinghe WMTN, and. Gunathilake WSS, (2018) Conducting polymer blends (polyaniline/polypyrrole) as counter electrode materials in dye sensitized solar cells. Ceylon J Sci 47(3):263–268. https://doi.org/10.4038/cjs.v47i3.7532
38. Muto T, Ikegami M, Miyasaka T (2010) Polythiophene-based mesoporous counter electrodes for plastic dye-sensitized solar cells. J Electrochem Soc 157(8):B1195–B1200. https://doi.org/10.1149/1.3447740
39. Xu H, Zhang X, Zhang C, Liu Z, Zhou X, Pang S, Chen X, Dong S, Zhang Z, Zhang L, Han P, Wang X, Cui G (2012) Nanostructured titanium nitride/PEDOT: PSS composite films as counter electrodes of dye-sensitized solar cells. ACS Appl Mater Interfaces 4:1087–1092. https://doi.org/10.1021/am201720p
40. Kumara GRA, Pitawala HMGTA, Karunarathne B, Mantilaka MMGPG, Rajapakse RMG, Huang HH, De SKH, Yoshimura M (2021) Development of a chemical-free floatation technology for the purification of vein graphite and characterization of the products. Sci Rep 11(1):22713. https://doi.org/10.1038/s41598-021-02101-9

41. Kay A, Gra¨tzel M, (1996) Low cost photovoltaic modules based on dye sensitized nanocrystalline titanium dioxide and carbon powder. Sol Energy Mater Sol Cell 44:99. https://doi.org/10.1016/0927-0248(96)00063-3
42. Kitamura K, Shiratori S (2011) Layer-by-layer self-assembled mesoporous PEDOT–PSS and carbon black hybrid films for platinum free dye-sensitized solar cell counter electrodes. Nanotechnology 22:195703. https://doi.org/10.1088/0957-4484/22/19/195703
43. Ng WC, Chong MN (2023) Organic-inorganic p-type PEDOT:PSS/CuO/MoS2 photocathode with in-built antipodal photogenerated holes and electrons transfer pathways for efficient solar-driven photoelectrochemical water splitting. Sustain Mater Technol 38:e00749. https://doi.org/10.1016/j.susmat.2023.e00749
44. Susanti E, Wulandari P, Herman (2018) Effect of localized surface plasmon resonance from incorporated gold nanoparticles in PEDOT:PSS hole transport layer for hybrid solar cell applications. J Phys Conf Ser 1080(1):012010. https://doi.org/10.1088/1742-6596/1080/1/012010
45. Banks CE, Davies TJ, Wildgoose GG, Compton RG (2005) Electrocatalysis at graphite and carbon nanotube modified electrodes: edge-plane sites and tube ends are the reactive sites. Chem Commun 829–841:829. https://doi.org/10.1039/B413177K
46. Jaafar H, Ahmada ZA, Ainb MF (2018) The use of carbon black-TiO_2 composite prepared using solid state method as counter electrode and E. conferta as sensitizer for dye-sensitized solar cell (DSSC) applications. Opt Mater 79:366–371. https://doi.org/10.1016/j.optmat.2018.04.008
47. Kouhnavard M, Ludin NA, Ghaffari BV, Sopian KI, Miyake M (2016) Hydrophilic carbon/TiO_2 colloid composite: a potential counter electrode for dye-sensitized solar cells. J Appl Electrochem 46(2):259–266. https://doi.org/10.1007/s10800-015-0910-4
48. Reich S, Thomsen C (2004) (2004) Raman spectroscopy of graphite. Phil Trans R Soc Lond A 362:2271–2288. https://doi.org/10.1098/rsta.2004.1454
49. Ferra A, Me J, Scardaci V, Casiraghi C, Lazzeri M, Mauri F, Piscanec S, Jiang D, Novoselov K, Roth S (2006) Raman spectrum of graphene and graphene layers. Phys Rev Lett 97:187401. https://doi.org/10.1103/PhysRevLett.97.187401
50. Lee WJ, Ramasamy E, Lee DY, Song JS (2009) Efficient dye-sensitized solar cells with catalytic multiwall carbon nanotube counter electrodes. Appl Mater Inter 1:1145–1149. https://doi.org/10.1021/am800249k
51. Du F, Cao NN, Zhang YF, Fu P, Wu YG, Lin ZD, Shi R, Amini A, Cheng C (2018) PEDOT:PSS/graphene quantum dots films with enhanced thermoelectric properties via strong interfacial interaction and phase separation. Sci Rep 8(1):6441. https://doi.org/10.1038/s41598-018-24632-4
52. Singhal P, Rattan S (2016) Swift heavy ion irradiation as a tool for homogeneous dispersion of nanographite platelets within the polymer matrices: toward tailoring the properties of PEDOT:PSS/nanographite nanocomposites. J Phys Chem B 120(13):3403–3413. https://doi.org/10.1021/acs.jpcb.5b11240
53. Popova AN (2017) Crystallographic analysis of graphite by X-ray diffraction. Coke Chem 60:361–365. https://doi.org/10.3103/S1068364X17090058
54. Xiaoyan P (2023) Study on preparation and properties of nanocrystalline TiO_2/graphite photocatalytic composite by mechanochemistry, Journal of Physics: Conference Series 2539 012057 IOP Publishing, https://doi.org/10.1088/1742-6596/2539/1/012057
55. Daikhin LI, Kornyshev AA, Urbakh M (1997) Double layer capacitance on a rough metal surface: surface roughness measured by "Debye ruler." Electrochim Acta 42:2853. https://doi.org/10.1016/S0013-4686(97)00106-0
56. Mukherjee S, Ramalingam B, Griggs L, Hamm S, Baker GA, Fraundorf F, Sengupta S, Gangopadhyay S (2012) Ultrafine sputter-deposited Pt nanoparticles for triiodide reduction in dye-sensitized solar cells: impact of nanoparticle size, crystallinity and surface coverage on catalytic activity. Nanotechnology 23:485405. https://doi.org/10.1088/0957-4484/23/48/485405
57. Dao VD, Hoon S, Choi KHS, Kim JH, Park HO, Lee JK (2011) Efficiency enhancement of dye-sensitized solar cell using Pt hollow sphere counter electrode. J Phys Chem C 115(51):25529–32553. https://doi.org/10.1021/jp208295b
58. Dao VD (2017) Comment on "Energy storage via polyvinylidene fluoride dielectric on the counter electrode of dye-sensitized solar cells" by Jiang et al. Journal of Power Sources, 337, 125, https://doi.org/10.1016/j.jpowsour.2016.10.100
59. Imotoa K, Takahashi K, Yamaguchi T, Komura T, Nakamura JI, Murata K (2003) High-performance carbon counter electrode for dye-sensitized solar cells. Solar Energy Mater Solar Cells 79:459–469. https://doi.org/10.1016/S0927-0248(03)00021-7
60. Farim F, Sikder A, Ghann W, Green K, Ozturk B, Ali MM, Uddin J (2020) Nanostructured dye sensitized solar cells with different counter electrodes. Am J Phys Chem 9(1):1–8. https://doi.org/10.11648/j.ajpc.20200901.11 (http://www.sciencepublishinggroup.com/j/ajpc)
61. Chou HT, Lien CH, Wu DH, Hsu HC and Huang MH (2013) The different film thicknesses of graphite/carbon black on the counter electrodes by spray coating method for dye-sensitized solar cells, 13th IEEE International Conference on Nanotechnology (IEEE-NANO 2013), Beijing, China, 2013, pp. 1151-1154, https://doi.org/10.1109/NANO.2013.6720989.
62. Xu S, Luo Y, Zhong W, Xiaoyun Liu X, Xiao Z, Luo Y (2013) Improved performances of graphite counter electrode for dye-sensitized solar cells by incorporating graphene nanosheets. Appl Mech Mater 253–255:689–692. https://doi.org/10.4028/www.scientific.net/AMM.253-255.689
63. Wu J, Wu S, Sun W (2021) Electropolymerization and application of polyoxometalate-doped polypyrrole film electrodes in dye-sensitized solar cells. Electrochem Commun 122:106879. https://doi.org/10.1016/j.elecom.2020.106879
64. Duan Y, Tang Q, Liu J, He B, Yu L (2014) Transparent metal selenide alloy counter electrodes for high-efficiency bifacial dye-sensitized solar cells. Angew Chem Int Ed 53:1–7. https://doi.org/10.1002/anie.201409422
65. Han L, Koide N, Chiba Y, Islam A, Komiya R, Fuke N, Fukui A, Yamanaka R (2005) Improvement of efficiency of dye-sensitized solar cells by reduction of internal resistance. Appl Phys Lett 86:213501. https://doi.org/10.1063/1.1925773g
66. Ahmed ASA, Xianga W, Hua X, Qia C, Amiinuc IS, Zhao X (2018) Si3N4/MoS2-PEDOT: PSS composite counter electrode for bifacial dye sensitized solar cells. Sol Energy 173:1135–1143. https://doi.org/10.1016/j.solener.2018.08.062
67. Wei TC, Wan CC, Wang YY, Chen CM (2007) Shiu HS (2007) Platinum a noparticles on flexible carbon fiber paper without transparent conducting oxide glass as counter electrode for dye-sensitized solar cells. J Phys Chem C 111:4827–4853. https://doi.org/10.1021/am101204f
68. Hussain S, Patil SA, Vikraman D et al (2018) Large area growth of $MoTe_2$ films as high performance counter electrodes for dye-sensitized solar cells. Sci Rep 8:29. https://doi.org/10.1038/s41598-017-18067-6
69. Yen MY, Yen CY, Liao SH, Hsiao MC, Weng CC, Lin YF, Ma CM, Tsai MC, Su A, Ho KK, Liu PL (2009) A novel carbon-based nanocomposite plate as a counter electrode for dye-sensitized solar cells. Comp Sci Technol 69:2193. https://doi.org/10.1016/j.rineng.2023.101611
70. Gnanasekar S, Kollu P, Jeong SJ, Grace AN (2019) Pt-free, low-cost and efficient counter electrode with carbon wrapped VO2(M)

nanofiber for dye sensitized solar cells. Sci Rep 9:5177. https://doi.org/10.1038/s41598-019-41693-1

71. Yang J, Bao C, Zhu K, Yu T, Li F, Liu J, Zou Z (2014) High catalytic activity and stability of nickel sulfide and cobalt sulfide hierarchical nanospheres on the counter electrodes for dye-sensitized solar cells. Chem Commun 50(37):4824–4826. https://doi.org/10.1039/c4cc00001c
72. Dao VD, Kim SH, Choi HS, Kim JH, Han-Oh Park HO, Lee JK (2011) Efficiency enhancement of dye-sensitized solar cell using Pt hollow sphere counter electrode. J Phys Chem C 115(51):25529–32553. https://doi.org/10.1021/jp208295b
73. Cheruku R, Kim JH, Krishna VBM, Periyat P, Duvvuri S (2023) Photo-electrodes decorated with carbon quantum dots: efficient dye-sensitized solar cells. Results Eng 20:101611. https://doi.org/10.1016/j.rineng.2023.101611
74. Daeneke T, Mozer AJ, Kwon TH, Duffy NW, Holmes AB, Bach U, and. Spiccia L, (2012) Dye regeneration and charge recombination in dye-sensitized solar cells with ferrocene derivatives as redox mediators. Energy Environ Sci 5:7090–7099. https://doi.org/10.1039/C2EE21257A
75. Zhu W, Zhao Y, Duan J, Duan Y, Tang Q, He B (2017) Carbon quantum dot tailored counter electrode for 7.01%-rear efficiency in a bifacial dye-sensitized solar cell. Chem Commun 53:9894–9897. https://doi.org/10.1039/c7cc05480g
76. Xu T, Kong D, Tang H, Qin X, Li X, Gurung A, Kou K, Chen L, Qiao Q, Huang W (2020) Transparent MoS_2/PEDOT composite counter electrodes for bifacial dye-sensitized solar cells. ACS Omega 5(15):8687–8696. https://doi.org/10.1021/acsomega.0c0017510.1021/acsomega.0c00175.s001
77. He B, Tang Q, Wang M, Chen H, Yuan S (2014) Robust polyaniline-graphene complex counter electrodes for efficient dye-sensitized solar cells. ACS Appl Mater Interfaces 6:8230–8236. https://doi.org/10.1021/am500981w
78. Wei P, Li J, Kang H, Hao Z, Yang Y, Guo D, Liu L (2019) Cost-effective and efficient dye-sensitized solar cells with nickel cobalt sulfide counter electrodes. Sol Energy 188:603–608. https://doi.org/10.1016/j.solener.2019.06.034
79. Yue G, Li F, Tan F, Li G (2014) Chena C and Wub J (2014) Nickel sulfide films with significantly enhanced electrochemical performance induced by self-assembly of 4-aminothiophenol and their application in dye-sensitized solar cells. RSC Adv 4:64068. https://doi.org/10.1039/c4ra10978c